

# Effects of Accident Thermal Loading on In-Plane Shear Behavior of Steel-Plate Composite Walls

Saahastaranshu R. Bhardwaj, Kadir C. Sener, and Amit H. Varma

---

## ABSTRACT

Structural walls in safety-related nuclear facilities are required to be designed for seismic and accident thermal (due to postulated high-energy pipe break events) loading combination. Current U.S. and international codes provide limited guidance for analysis and design of walls for this loading combination. This paper describes the experimental results and observations from tests conducted on a laboratory-scale (1:4 to 1:5) test unit representing steel-plate composite (SC) walls subjected to combined in-plane (seismic) and accident thermal loading. The test unit was subjected to surface temperatures of up to 450°F in combination with cyclic in-plane loading. Results of similar experiments recently conducted in Japan are also summarized (with surface temperatures up to 570°F). Surface heating combined with the low thermal conductivity and high specific heat of concrete resulted in nonlinear thermal gradients through the thickness of the specimens. These nonlinear thermal gradients and the associated self- or internal restraint led to extensive concrete cracking. This concrete cracking reduced the initial and secant stiffness of the specimens. The initial stiffness of the heated specimens reduced to 30 to 40% of the initial stiffness of the control (unheated) specimen. The secant stiffness of the heated specimens reduced up to 50% of the secant stiffness of the control (unheated) specimen. However, the in-plane shear strength of the heated SC specimens was still approximately 10 to 30% greater than the nominal in-plane shear strength calculated, for the limit state of steel plate von Mises yielding, using AISC N690 equations and measured material properties. Evaluation of the experimental results and observations suggests that the in-plane shear strength of SC walls subjected to typical accident surface temperatures (up to 570°F) can be estimated conservatively using the current provisions of AISC N690. The stiffness for accident thermal loading combinations can be considered to reduce from cracked composite stiffness at ambient temperature to fully cracked—that is, steel-only stiffness as the surface temperature increases up to typical accident value.

**Keywords:** steel-plate composite, structural walls, accident thermal, seismic, in-plane shear, shear stiffness, flexural stiffness.

---

## INTRODUCTION

Structural walls in safety-related facilities may be a part of labyrinthine structures (with cross-walls, typical to nuclear construction), or stand-alone shear walls [typical in Department of Energy (DOE)-type nuclear facilities or commercial construction]. These structural walls may be reinforced concrete (RC) or steel-plate composite (SC) walls depending on the overall structure or plant design. While RC walls have been traditionally used, SC structures are also being used for the third generation of nuclear power plants and being considered for small modular reactors (SMR) of the future. SC walls are comprised of structural

steel modules filled with plain concrete. The modules consist of two steel faceplates that form the opposite surfaces of the wall and define its total thickness. The faceplates are connected to each other using ties spaced uniformly in both the vertical and horizontal directions. These ties consist of steel rods or structural shapes (angles, channels, plates, etc.) that are typically welded to the steel faceplates. The ties provide structural stability during transportation, handling, and erection. Steel headed stud anchors may be welded to the interior surfaces of the steel faceplates. Stud anchors and/or ties provide composite action, faceplate local buckling restraint, and anchorage to the infill after concrete placement. The ties also provide composite action and anchorage to the concrete infill and serve as out-of-plane shear reinforcement for the composite SC walls. The steel modules—consisting of faceplates, ties, and stud anchors—can be prefabricated in the shop, transported to the site, assembled into larger modular structures, and then filled with plain concrete, thus leveraging modular construction approaches to expedite construction schedule and optimize overall project costs (NRC, 2011, 2012; Schlaseman and Russell, 2004).

Advantages of modular SC walls in terms of structural efficiency and construction economy (Varma et al., 2015; Sener et al., 2015b; Booth et al., 2015; Bruhl et al., 2015;

---

Saahastaranshu R. Bhardwaj, Assistant Professor, University of Alabama, Tuscaloosa, Ala. Email: saahas.bhardwaj@ua.edu (corresponding author)

Kadir C. Sener, Assistant Professor, Auburn University, Auburn, Ala. Email: sener@auburn.edu

Amit H. Varma, Karl H. Kettelhut Professor and Director of Bowen Laboratory, Purdue University, West Lafayette, Ind. Email: ahvarma@purdue.edu

---

Paper No. 2022-05

Bruhl and Varma, 2018) have led to the SC walls being considered for commercial construction. There has been recent research on the commercial building application of SC walls with boundary elements (Selvarajah, 2013; Bruneau et al., 2013; Ji et al., 2017; Varma et al., 2017). The current building codes, namely, ASCE 7 (ASCE, 2022) and AISC 341 (AISC, 2016), permit the use of composite plate shear walls-concrete filled (C-PSW/CF), with boundary elements, in seismic regions (Bruneau et al., 2013; Alzeni and Bruneau, 2014).

There are some significant differences between SC walls used in safety-related nuclear facilities and those used in commercial building projects. Safety-related nuclear facilities are labyrinthine in plan and consist of numerous cross-connecting, intersecting, squat (or short) SC walls with height-to-length ratios less than 1.0. There are typically no other structural frames or lateral force-resisting systems besides this network of SC walls. Commercial building structures typically use steel gravity frames and a lateral force-resisting system for wind and seismic loads. The lateral-force resisting system may consist of individual SC walls (with or without boundary elements) as distributed shear walls or coupled composite SC shear walls with adequate coupling action. In both cases, the SC walls are tall slender structures with height-to-length ratios greater than 3.0 and are governed by their in-plane flexure behavior. Another major difference is that SC walls in safety-related nuclear facilities have to be designed for the accident thermal plus seismic loading combination as specified in the *Code Requirements for Nuclear Safety-Related Concrete Structures and Commentary* (ACI 349, 2013), the *Specification for Safety-Related Steel Structures for Nuclear Facilities* (AISC N690, 2018), and the U.S. Nuclear Regulatory Commission's RG 1.142 (NRC, 2020) and RG 1.243 (NRC, 2021). During this challenging design-basis load combination, the facility is expected to shut down safely, which requires all the equipment to function and the structure to respond with limited inelastic deformations. The SC structure stiffness and strength during the combined accident thermal plus seismic loading combination are required to check the structure design strength against the design demands calculated using appropriate models and to verify the in-structure response spectra for equipment performance. The Fukushima nuclear accident of 2011 emphasized the importance of this design-basis load combination. Although the probability of multiple design-basis events occurring simultaneously is low, severe impact of one hazard may trigger other hazards; for example, earthquake shocks may lead to accident thermal events. Subsequent aftershocks (potentially as intense as the main shock) may occur during the accident thermal event. This load combination of accident thermal loading and safe shutdown earthquake (SSE) also presents a significant design challenge for

small modular reactors (SMRs) since postulated accident scenarios may cause higher magnitudes of elevated temperatures for longer durations in their smaller constrained spaces.

Current design codes and standards offer limited procedural guidance for including the effects of accident thermal loading on seismic behavior (stiffness, strength, ductility, or reserve margin) of structures. Existing research focuses on the individual effects of either seismic or accident thermal loading, but not the combination of these loads. There is a need to develop design guidelines (based on experimental and numerical studies) for structural walls subjected to combined accident thermal and seismic loading.

This paper presents an experimental evaluation of the seismic (in-plane) behavior of squat SC wall specimens (with boundary elements) subjected to typical accident temperatures for Generation III pressurized water reactors (PWRs). Since the behavior of SC walls (with boundary elements or flanges, which may be cross-SC walls or closure steel flange plates, as seen in Figure 3) is fundamentally different from the behavior of SC wall piers (without boundary elements) (Kurt et al., 2016), the evaluation of SC wall piers for combined seismic and thermal loading is presented in Bhardwaj et al. (2019a). The authors have also conducted similar studies for RC beams (Sener et al., 2019a) and RC walls (Bhardwaj et al., 2018; Anwar et al. 2019). This paper first discusses relevant research conducted on SC walls subjected to individual hazards like seismic and accident thermal loads. Recent experimental studies conducted in Japan on SC walls subjected to combined thermal and seismic loading are also summarized. The paper then discusses the experimental studies conducted by authors in detail. This discussion includes the experimental approach, setup, test unit design and testing procedure, and instrumentation layout. The experimental measurements, results, and observations are used to evaluate the performance of SC walls. Results of experiments conducted by the authors, and findings reported by Japanese researchers are compared with current specifications for design of SC walls in safety-related nuclear facilities, AISC N690 (2018). These results are used to develop stiffness and strength recommendations for SC walls subjected to combined seismic and thermal loads.

## BACKGROUND

In the past, experimental and numerical research was conducted to evaluate the response of SC walls to seismic (in-plane) loading. Numerical studies were conducted to investigate the effect of accident thermal loading on SC structures. The existing body of research on the in-plane response of SC walls, and material and structural response to accident thermal loading are discussed in this section.

## In-Plane Loading

For SC walls, in-plane flexure (bending moment) is primarily resisted by the boundary elements (flanges—e.g., cross SC walls or steel flange plates). In-plane shear is resisted primarily by the web of the wall. The in-plane shear behavior of SC walls was developed by Ozaki et al. (2004) and extended by Varma et al. (2014). The in-plane behavior can be represented by a tri-linear shear force–strain ( $S_{xy}$ – $\gamma_{xy}$ ) curve. As described in Ozaki et al. (2004) and Seo et al. (2016), the in-plane response of SC walls can be defined by a mechanics-based behavior model (MBM) that uses composite plate theory. The in-plane behavior was idealized into three parts: (1) before concrete cracking, where concrete and steel plates are elastic and perfect bond between them can be assumed; (2) post-cracking, where cracks form in the concrete while steel plates remain elastic; and (3) post-yield, where faceplates undergo von Mises yielding. The in-plane shear strength (based on von Mises yielding) and stiffness (tripartite stiffness) requirements in AISC N690 (2018) are based on the trilinear MBM. Seo et al. (2016) verified the tri-linear curve using a large in-plane shear test experimental database and observed that AISC N690 equations estimated the in-plane strength conservatively.

Booth et al. (2020) demonstrated that SC walls have additional in-plane strength beyond the von Mises yielding of faceplates. The authors provided mechanics-based equations for calculating the ultimate in-plane shear strength,  $V_u$ , of SC walls. This additional post-yield shear resistance is provided by the concrete compression strut (concrete arch action) that develops along the compression diagonal and is anchored into the boundary elements. The post-yield strength contribution depends on the compression capacity of the concrete diagonal strut, which is subjected to crack opening by the transverse tensile strain field, and the strength of the boundary elements and the connection between the wall (web) and boundary elements to anchor and resist the thrust being delivered by the concrete compression diagonal strut.

## Thermal Loading

Structural walls in safety-related nuclear facilities may be subjected to accident thermal loads due to postulated high-energy pipe break events in pressurized water reactors. These accidents result in thermal and pressure loading on the walls. This article focuses on the effect of thermal loading on the in-plane shear behavior of SC walls. Accident pressures may result in out-of-plane loading on the walls. Behavior of SC wall piers under biaxial loading (in-plane and out-of-plane loading) is discussed elsewhere in Bhardwaj et al. (2019b). For accident thermal loading, thermal-hydraulic analyses are conducted to estimate the temperature histories ( $T$ - $t$  plots) for the surfaces of walls

exposed to accidents. Sener et al. (2015a) identified and developed typical accident temperature-time histories for the containment internal structure of pressurized water reactors using the envelopes of  $T$ - $t$  histories published in design control documents for various plant designs. The  $T$ - $t$  curves used for this experimental study were representative of these typical accident temperature-time histories.

The surface  $T$ - $t$  curve, and concrete and steel thermal properties govern the evolution of the through-thickness nonlinear thermal gradients for the walls. The thermal and mechanical properties of steel and concrete depend on the associated temperature. Significant research has been conducted on the change in steel and concrete properties at elevated temperatures (Hong and Varma, 2009; Naus, 2009; Takeuchi et al., 1993; Kodur et al., 2010). However, most of the research has focused on elevated temperatures associated with fire scenarios that are significantly higher (1500–1800°F) than typical accident temperatures (up to 570°F) in safety-related nuclear facilities. The recommendations for steel and concrete material properties at elevated temperatures are provided in Eurocode 2 and 3 (CEN, 2004, 2005) and AISC N690 (AISC, 2018). For the range of accident temperatures (up to 572°F), the steel yield and tensile strength values do not reduce. However, the steel stress-strain curves become nonlinear before reaching the yield plateau, and this nonlinearity increases with increase in temperature. The modulus of elasticity of steel reduces by about 20% as the temperature increases from ambient, 68°F, to 572°F. Unlike steel, the concrete compression strength reduces considerably for the range of accident thermal temperatures. While there is no reduction for temperatures up to 212°F, the compressive strength reduces by 10% for 390°F and by 15% for 572°F. Additionally, the reduction in initial modulus of elasticity is higher for concrete than that for steel. The modulus of elasticity of concrete in compression reduces by 40% as concrete temperature increases from ambient, 68°F, to 572°F. Material properties such as the thermal conductivity, specific heat, and thermal expansion are also provided as functions of elevated temperatures in Eurocode 2 and 3.

Thermal loading on structures results in internal stresses in the walls. These thermal stresses differ from stresses generated by mechanical loads in the sense that they are generated by restraints against thermal deformations rather than to equilibrate applied loads. Thermally induced internal stresses are self-relieving—that is, thermal (tensile) stresses can be relieved as the restraint reduces due to concrete cracking, reinforcement yielding, creep, and relaxation. Bhardwaj et al. (2015) discussed the effect of accident thermal loads (from postulated pipe break scenarios) on the structural behavior of wall structures, and the evolution of through thickness nonlinear thermal gradients for accident thermal loads. During the first few hours (up to one day)

of the thermal accident, structural members are subjected to significantly nonlinear thermal gradients through the thickness. These nonlinear thermal gradients induce concrete cracking due to internal or self-restraint (Sener et al., 2019a; Bhardwaj et al., 2015). After the first few days of the accident, the thermal gradients become relatively uniform through the thickness. The concrete crack widths, produced during the first few hours due to self-restraint, may reduce or even close due to the uniformity of temperatures (elimination of nonlinear gradient and corresponding internal restraint) through the thickness. Additionally, the uniform temperature magnitudes are lower than the maximum values reached earlier. However, the concrete does not regain its uncracked stiffness for mechanical loads.

This structural response to thermal loads was numerically validated by Bhardwaj et al. (2015), by subjecting 48 in. thick RC structures to idealized  $T-t$  curves. The response was also experimentally verified by Vecchio and Sato (1990) on an RC portal frame structure that was subjected to surface temperature change of up to 144°F from one side. The experimental results indicated that the internal forces, strains, and deformations (demands) induced by thermal loading were largest shortly after the peak surface temperatures were attained, when the nonlinearity in the thermal gradient was greatest. The thermally induced demands gradually reduced as the through-depth thermal gradient became uniform with continued heating. The test results also verified that thermally induced concrete cracking was observed in the externally unrestrained sections of the portal frame due to the internal restraints to free thermal expansion associated with the nonlinear temperature gradient. The mechanical load test results performed following thermal loading showed that the frame response was in accordance with the cracked section stiffness, and uncracked section stiffness overestimated the response significantly. Recently, Sener et al. (2019a) subjected six reinforced beam specimens to different combinations of accident thermal and out-of-plane shear loadings. The beam specimens had two different clear covers (0.75 in. and 1.5 in.), two surface temperature magnitudes (300°F and 450°F), and different heating locations (two-sided vs. one-sided, shear span vs. constant-moment region). The authors observed that section shear stiffness reduced due to thermal loading. Lower clear cover or higher surface temperatures resulted in measured shear strength values marginally lower than those calculated per ACI 349 (2013).

## PREVIOUS STUDIES

Kitajima et al. (2017) have conducted experimental studies on the seismic behavior of squat (shear-critical) SC walls subjected to accident thermal loading. Details of the specimens (Specimens 2, 3, 4, 5, and 7) are presented in Table 1.

The table includes the specimen height ( $h$ ), length ( $l_w$ ), thickness ( $T$ ), faceplate thickness ( $t_p$ ), flange plate thickness ( $t_f$ ), aspect ratio, faceplate reinforcement ratio ( $\rho = 2t_p/T$ ), faceplate stud spacing ( $s/T$ ), faceplate slenderness ratio ( $s/t_p$ ), flange plate slenderness ratio ( $s_f/t_f$ ), tie spacing ( $S/T$ ), faceplate ( $F_{yw}$ ) and flange plate ( $F_{yf}$ ) yield strengths, concrete compressive strength ( $f'_c$ ), maximum surface temperature ( $T_{max}$ ), lateral loading protocol (cyclic or monotonic), and duration of heating for the specimens. The tested specimens were 1:7 scale models of SC walls for the containment vessel structure. The specimens had a height-to-length ratio of 1.0, wall thickness of 11.2 in., steel faceplate thickness of 0.091 in., and flange plate (end plate) thickness of 0.87 in. The specimens were restrained against rotation at top and bottom, resulting in a shear aspect (moment-to-shear) ratio of 0.5.

These identical specimens were tested for different combinations of lateral and accident thermal loading, including (1) monotonic lateral loading at ambient temperature (Specimen 2, Control specimen); (2) monotonic lateral loading with accident temperature of 293°F, heated for 30 days (Specimen 3); (3) cyclic lateral loading with accident temperature of 293°F, heated for 30 days (Specimen 4); (4) monotonic lateral loading with accident temperature of 347°F, heated for 60 minutes (Specimen 5); and (5) monotonic lateral loading with accident temperature of 572°F, heated for 30 days (Specimen 7). The measured concrete compressive strengths,  $f'_c$ , for the specimens are presented in Table 1. Kitajima et al. (2017) did not report the measured strengths for steel plates. However, the measured properties for the plate material used (SPV 490) were reported in a companion paper (Hirama et al., 2015) and have been included in Table 1.

Table 2 summarizes the measured lateral strength,  $V_{n-ip}$ , initial stiffness,  $K_{in}$ , and secant stiffness,  $K_{sec}$ , for specimens tested by Kitajima et al. (2017). The table also shows the reduction in strength and initial,  $K_{in}$ , and secant,  $K_{sec}$ , stiffnesses of the heated specimens in comparison with those of the ambient (control) specimen, Specimen 2. For example,  $V_{n-ip}/V_{n-ip-2}$  is the ratio of measured strength of the heated specimens with respect to that of the control Specimen 2. A reduction of 15–30% in lateral strength,  $V_{n-ip}$ , of the heated specimens was observed with respect to the strength for control specimen. In spite of this reduction, the lateral strengths of the heated specimens were greater than the nominal strength calculated using measured properties and the AISC N690 (2018) equation for in-plane shear strength ( $V_n^{AISC}$ , corresponding to von Mises yielding of faceplates), with a safety margin ranging from 9% to 36% (as seen in Table 4, discussed later).

The initial stiffness of the heated specimens was reduced to 30–40% of the initial stiffness of the ambient (Control) Specimen 2. This significant reduction in initial stiffness

**Table 1. Specimen and Test Unit Details**

Identifier <sup>1</sup>	Height, $h$ (in.)	Length, $l_w$ (in.)	Thickness, $T$ , (in.)	Faceplate Thickness, $t_p$ (in.)	Flange Plate Thickness, $t_f$ (in.)	Aspect Ratio	Faceplate Reinforcement Ratio, $\rho$	Faceplate Stud Spacing, $s/T$	Faceplate Slenderness Ratio, $s/t_p$	Flange Plate Slenderness Ratio, $s_f/t_f$	Tie Spacing, $S/T$	Faceplate $F_{yw}$ (ksi)	Flange Plate $F_{yf}$ (ksi)	Concrete $f'_c$ (ksi)	Lateral Loading <sup>2</sup>	Maximum Surface Temperature, $T_{max}$ (°F)	Duration of Heating (hours)
2														6.7	M	Ambient	NA
3														5.9	M	293	720
4	27.6	27.6	11.2	0.091	0.87	0.5 <sup>#</sup>	0.016	0.16	20	2.1	N.A.	103	103	6.9	C	293	720
5														6.1	M	347	1
7														5.5	M	572	720
SC-W-H	36 <sup>3</sup>	48	10	0.104	0.75	0.75	0.021	0.25	24	3.33	0.5	57	60	6.4	C	300 and 450	1 and 3

<sup>1</sup> Specimens 2–5 and 7 were tested by Kitajima et al. (2017); test unit SC-W-H was tested by the authors.  
<sup>2</sup> Lateral loading: M = monotonic, C = cyclic.  
<sup>3</sup> Corresponds to lateral loading location.  
<sup>#</sup> Specimens were restrained against rotation at top and bottom, resulting in a shear aspect (moment-to-shear) ratio of 0.5.

Specimen	$T_{max}$ (°F)	$V_{n-ip}$ (kips)	$K_{in}$ (kips/in.)	$K_{sec}$ (kips/in.)	$V_{n-ip}/V_{n-ip-2}$	$K_{in}/K_{in-2}$	$K_{sec}/K_{sec-2}$
2	Ambient	790	8800	3630	1.00	1.00	1.00
3	293	561	3650	2330	0.71	0.41	0.64
4	293	699	3120	2330	0.88	0.35	0.64
5	347	600	2790	2090	0.76	0.32	0.58
7	572	609	2510	1870	0.77	0.29	0.52

is attributed primarily to the concrete cracking caused by the thermal loads and the slight reduction in the elastic and shear moduli of steel and concrete materials, as discussed previously. The secant stiffness of the heated specimens was calculated at 60% of the peak load for the control Specimen 2. The secant stiffness of the heated specimens reduced to about 50–60% of the secant stiffness of the ambient Specimen 2. While Specimens 3 and 4 had similar stiffness reductions, the reduction in strength for the monotonically loaded specimen (Specimen 3) was greater than that for the specimen with cyclic loading (Specimen 4), which was an unexpected result.

Most of the specimens tested by Kitajima et al. (2017) were subjected to heating, while maintaining surface temperatures at the target value, for 30 days (except Specimen 5, for which the heating duration was only 60 minutes). Because the specimens were scaled (1:7 scale), the heating duration of 30 days will actually correspond to several months of accident temperature for the physical structure, which is not representative of the accident scenarios. The probability of powerful aftershocks (potentially as intense as the main shock), during or after a thermal accident initiated by a seismic event, is highest during the first few hours after the main seismic event. Therefore, the accident durations should be scaled for the specimens to better simulate the nonlinear thermal gradient history. The duration of heating (30 days) for the scaled specimens tested by Kitajima et al. (2017) would have resulted in uniform temperature through the thickness [based on the discussion in Bhardwaj et al. (2015)], which is not representative of the critical state (with nonlinear thermal gradient) for the wall. Kitajima et al. (2017) also do not provide any information about the reduction in the shear stiffness of these (shear-critical) specimens due to accident thermal temperatures.

To address these concerns, and to supplement the knowledge obtained from the tests by Kitajima et al. (2017), the authors conducted experiments to evaluate the ambient stiffness and the stiffness and strength of SC walls for combined thermal and seismic loading. The experiments were designed to evaluate the effects of different magnitudes and durations of accident temperatures on the stiffness and strength of SC walls. Instrumentation layout was designed

to calculate the secant wall stiffness and the component shear and flexural stiffnesses of the SC walls for ambient and accident thermal conditions.

## DESIGN OF EXPERIMENTS

This section discusses the design of the test unit, the experimental setup and procedure, and the instrumentation layout for the tests conducted by the authors.

### Design of Test Unit

Table 1 presents the details of the SC wall test unit (SC-W-H) subjected to combinations of accident thermal and seismic loading protocols. The faceplate and flange plate slenderness ratios were designed to meet the limits recommended by AISC N690 (2018)—that is, to develop yielding in compression before local buckling, based on Zhang et al. (2014). The test unit had a shear aspect (wall height-to-length) ratio of 0.75, and the flange plate thickness was designed to ensure that the specimen has a shear-critical response similar to squat walls in safety-related nuclear facilities. Three-dimensional nonlinear inelastic finite element models were developed for the specimen tested by Kitajima et al. (2017) and analyzed using ABAQUS (Simulia, 2014). The modeling details are provided in Sener et al. (2019b) and Bhardwaj (2018), and not repeated here for brevity. Figure 1(a) compares the results from the finite element analysis of Specimen 2 with the lateral force-deformation response reported from the test conducted under monotonic loading. The figure also includes horizontal lines corresponding to the in-plane shear strength,  $V_n^{AISC}$ , and in-plane flexural capacity,  $M_{ny}$ , of the wall. The in-plane shear strength was calculated using Equation A-N9-20 in AISC N690 (2018), and the in-plane flexural capacity was calculated using the plastic stress distribution method in Section NI.2 of AISC N690, both while using measured material properties. As shown in Figure 1(a), the stiffness and strength estimated by the numerical model compared favorably with the experimental results. The benchmarked modeling approach was then used to predict the behavior and finalize the design of the SC wall test unit. The numerical models considered

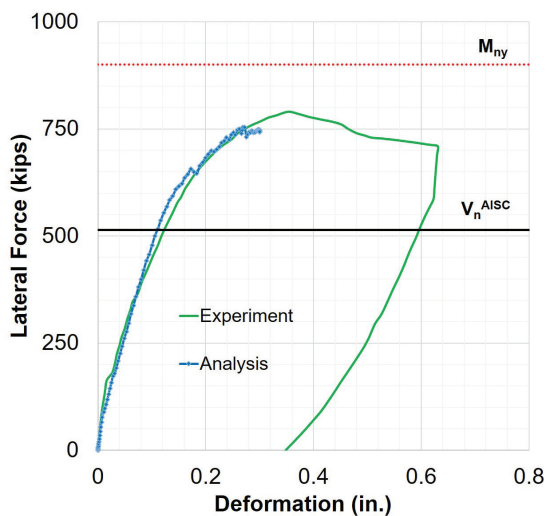
60 ksi yield strength for both the faceplates and the flange plates. The flange plate thickness of the SC wall test unit was varied to evaluate behavior and to ensure that the test unit with wall aspect ratio of 0.75 was shear critical—that is, have lateral loading corresponding to in-plane flexural strength greater than that corresponding to in-plane shear strength. As shown in Figure 1(b), three different thicknesses for flange plates were used in the models (0.50, 0.75, and 1.00 in.). A comparison of these responses indicated that 0.75 in. flange plate thickness provided sufficient flexural capacity for the test unit to be shear critical and was, therefore, used for SC-W-H.

### Loading and Heating Protocols

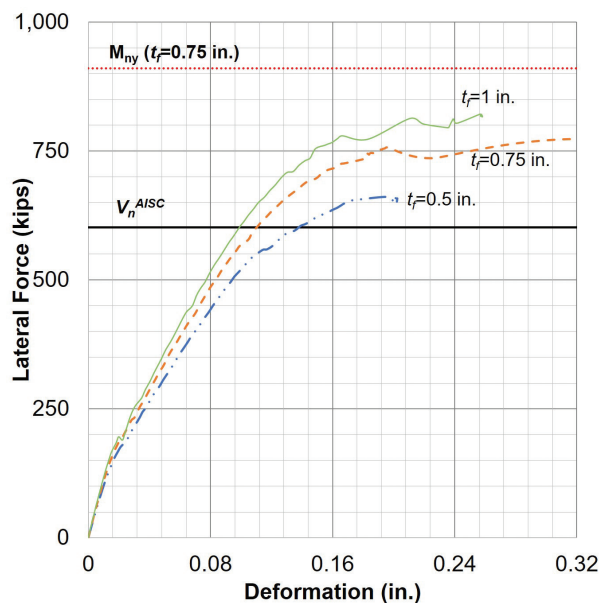
Table 3 summarizes the loading and heating protocols for the test unit SC-W-H. Similar protocols were employed for SC wall pier and RC wall units tested by the authors (Bhardwaj et al., 2018, 2019a, 2019b). The test unit was subjected to two surface temperature magnitudes (300°F and 450°F), and force/displacement cycles at heating durations of 1 hr and 3 hr. The temperature magnitudes were based on typical containment internal structure (CIS) surface time-temperature histories for postulated pipe break scenarios as obtained from public domain documents (discussed in Sener et al., 2015a). These temperature magnitudes are also consistent with those used by Kitajima et al. (2017). Based on the discussion in Bhardwaj et al. (2015): (1) 1 hr heating duration was selected to develop significant nonlinear

thermal gradient (resulting in extensive concrete cracking) through the cross section, and (2) 3 hr heating duration was selected to reduce the nonlinearity of thermal gradients through the cross section (potentially reducing the crack widths). These heating durations (of 1 and 3 hr) result in through thickness temperature profiles in the scaled test unit (1:3 to 1:4 scale) similar to those observed in full-scale (36- to 48-in.-thick) walls. The test unit was cooled down to ambient temperature after completing the load cycle at 3 hr of heating and then heated-loaded to the next temperature-load level.

Figure 2 presents the loading and heating time history for test unit SC-W-H. The loading and heating cycles are plotted together against the duration of testing (for clarity, the time for the test unit to cool down between heating cycles has not been plotted). Loading cycle numbers are also mentioned in the figure. As shown in Table 3 and Figure 2, the first three load cycles were performed at ambient temperature and load levels corresponding to 25, 50, and 75% of the estimated test unit strength,  $F_n$  (Cycles 1, 2, and 3, respectively).  $F_n$  was the force corresponding to nominal in-plane shear strength (using measured properties) of the test unit, based on AISC N690 (2018). These initial cycles were performed to investigate the ambient response of the wall pre- and post-cracking and before faceplate yielding and to compare the ambient response with responses (obtained in later cycles) for thermal loading. The ambient cycles were followed by heated cycles, where the faceplates and flange plates were heated to a surface temperature of



(a) Lateral load-deformation response of Specimen 2 from Kitajima et al. (2017)



(b) Comparison of lateral load-deformation response of proposed SC wall test unit

Fig. 1. Benchmarking analysis for design of SC-W-H test unit.

Cycle No.	Surface Temperature (°F)	Heating Duration (hours)	Target Force/ Displacement Level
1	Ambient	NA	$0.25F_n$
2	Ambient	NA	$0.5F_n$
3	Ambient	NA	$0.75F_n$
4	300	1	$0.75F_n$
5	300	3	$0.75F_n$
6	450	1	$0.75F_n$
7	450	3	$0.75F_n$
8	450	1	$1.0\Delta_y$
9	450	3	$1.0\Delta_y$
10	Ambient	NA	$1.0\Delta_y$
11	450	1	$1.5\Delta_y$
12	450	3	$1.5\Delta_y$
13	Ambient	NA	$1.5\Delta_y$
14	450	1	$2.0\Delta_y$
15	450	3	$2.0\Delta_y$

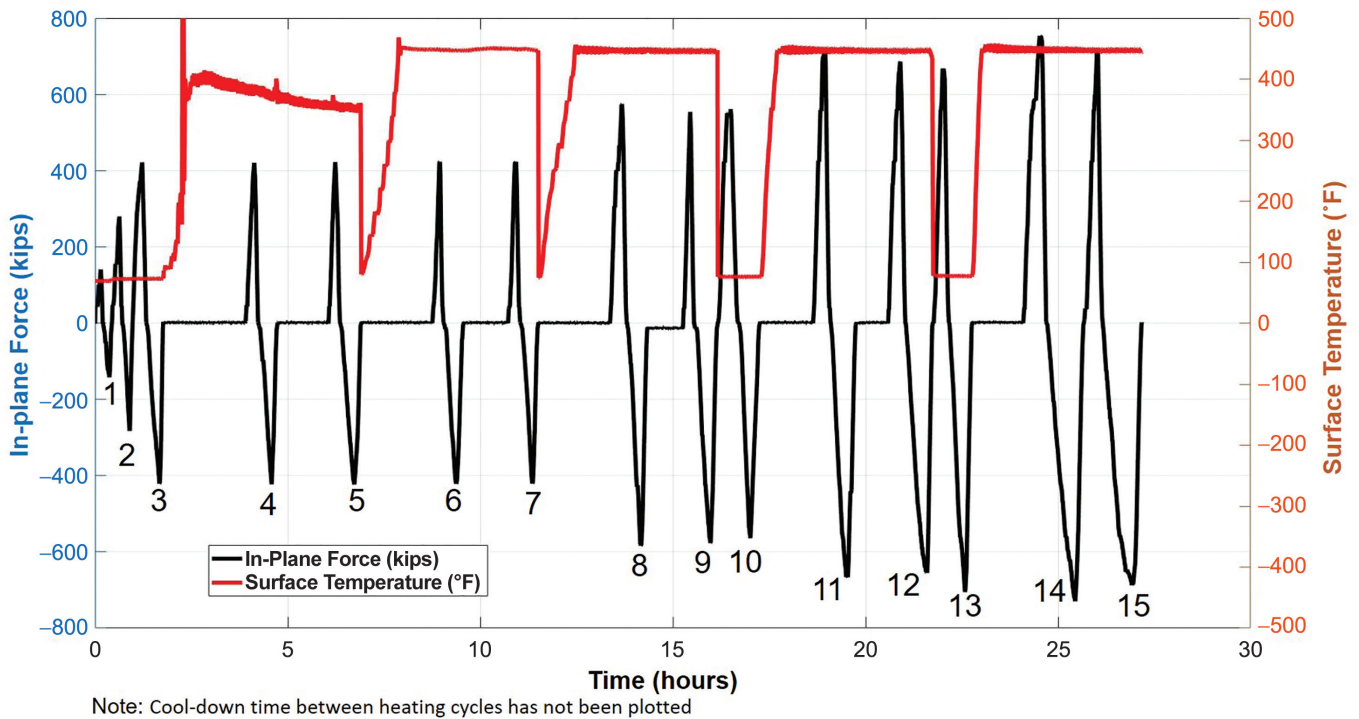


Fig. 2. Load and temperature time history for test unit SC-W-H.

300°F for 1 and 3 hr (Cycles 4 and 5, respectively; some regions of the wall were subjected to surface temperatures between 350 and 400°F). Similar heated cycles were conducted for surface temperature of 450°F (Cycles 6 and 7). The cycles that followed (Cycle 8 onward) were conducted in displacement control. Yield displacement ( $\Delta_y$ ) was estimated as the displacement corresponding to nominal yield load ( $F_n$ ) of the test unit, based on the average secant stiffness observed in Cycles 6 and 7. The test continued with thermal and displacement cycles at  $1.0\Delta_y$  (Cycles 8 and 9) and  $1.5\Delta_y$  (Cycles 11 and 12). Additional ambient loading cycles (10 and 13) were performed after the heated cycles at target displacement levels of  $1.0\Delta_y$  and  $1.5\Delta_y$  to determine if the stiffness increased after cooling. After the  $1.5\Delta_y$  cycles, the test unit was subjected to  $2.0\Delta_y$  (Cycles 14 and 15) cycles with surface temperatures maintained at 450°F for heating durations of 1 and 3 hr.

### Test Setup

Figure 3 shows a photograph of the test unit and setup (without heaters) in Bowen Lab. Lateral loading was applied using two 660-kip-capacity, double-acting, 12 in. stroke hydraulic actuators, which were post-tensioned to the laboratory reaction wall through a clevis-and-pin detail and a built-up wall box. The actuators applied lateral loading through loading beams that were bolted to the test unit. The steel assembly for the test unit (with flange plates, faceplates, studs, and ties) was fabricated, welded to a reusable baseplate foundation, and concrete was poured into the steel assembly. The steel baseplate was 60 in. long, 21.375 in. wide, and 1 in. thick. The baseplate had sixty  $\frac{3}{8}$ -in.-diameter shear studs (in three rows) on the top surface to transfer the forces from concrete infill to the baseplate. The baseplate was anchored to a concrete foundation block using 85 A706 #6 rebar that

were 47 in. long. The rebars were attached to the baseplate using Lenton C3J welded couplers.

The foundation block was post-tensioned to the strong floor using sixteen  $\frac{1}{4}$ -in.-diameter DYWIDAG bars, each post-tensioned to 250 kips. The wall-to-basemat connection was designed in accordance with AISC N690 (2018) and following AISC Design Guide 32 (Bhardwaj and Varma, 2017) to be 25% stronger than the wall, and thus limit inelastic deformations, yielding, failure, etc., to the wall portion outside of the wall-to-basemat connection. The wall-to-basemat connection included the steel faceplate-to-baseplate welded connection, the steel flange plate-to-baseplate welded connection, the wall concrete infill-to-baseplate connection achieved using shear stud anchors, and the steel baseplate-to-concrete basemat connection achieved using rebar anchors welded to the baseplate and embedded (fully developed) into the concrete foundation block. Thermal loading was applied to the faceplates and the flange plates (region between the loading beams and baseplate on the foundation block in Figure 3) using ceramic fiber radiant heating panels that were powered and controlled by a custom-built control system described in detail in Bhardwaj (2018).

### Instrumentation of Test Unit

Instrumentation layout for the test unit is presented in Figure 4. Displacement sensors [SPs in Figure 4(b)] were used to measure the lateral displacement at the loading location and bottom of the wall. The displacement measurements were used to obtain lateral force-displacement response of the test unit, base slip corrections (and to calculate the flexural deformation of the SC wall). Rotation meters (clinometers) were installed at the base of the wall in the in-plane [CM1 and CM2 in Figure 4(b)] direction. The in-plane

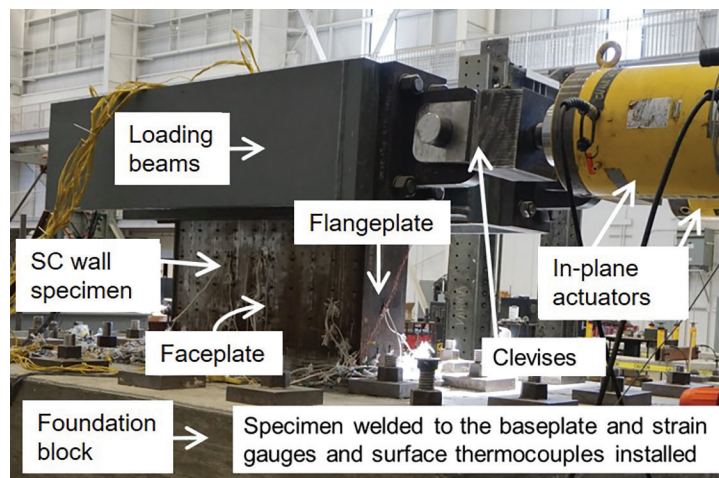
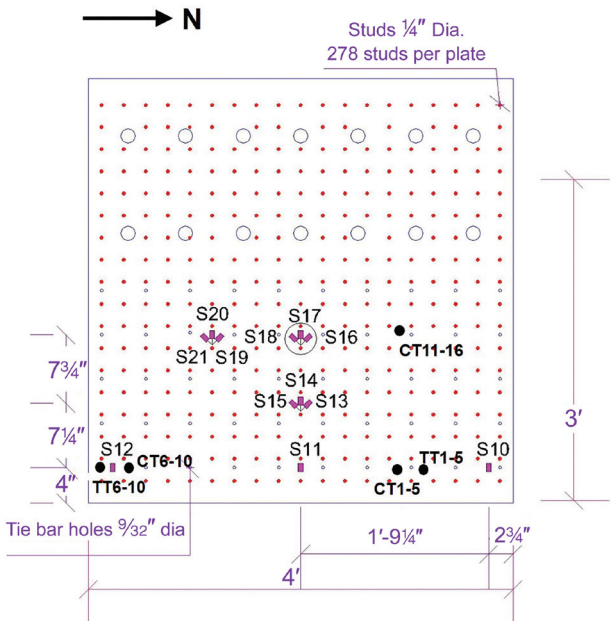


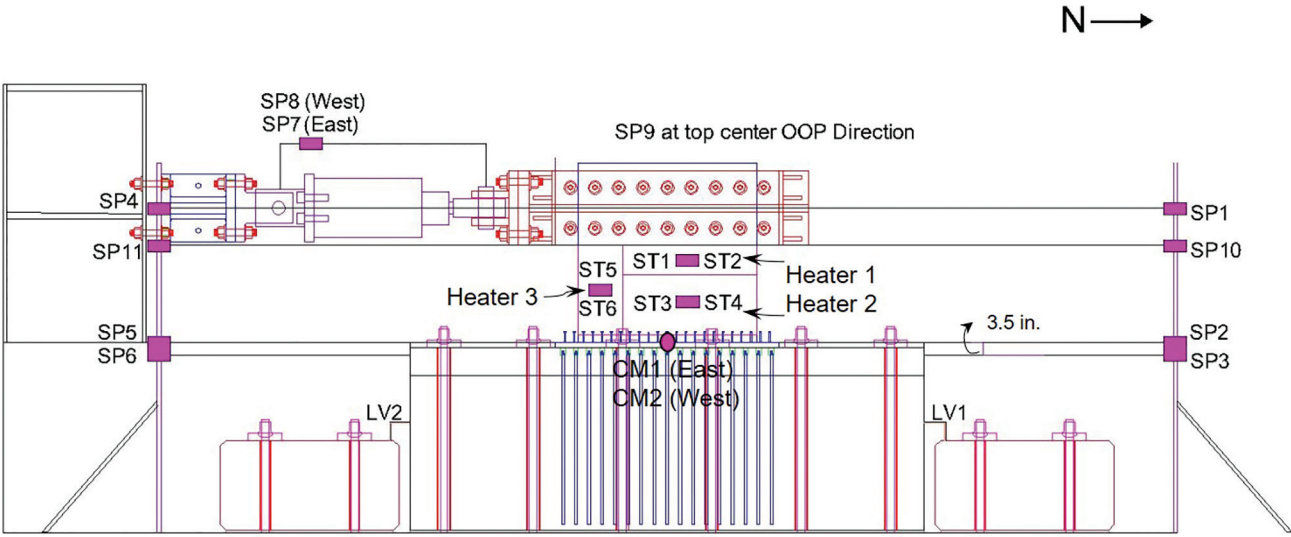
Fig. 3. Test unit and setup (without heaters).

rotation data was used to apply base rotation corrections to in-plane force-displacement plots [to subtract the rigid body displacement (due to base rotations) from the measured displacements]. High-temperature strain gauges were installed on the faceplates to evaluate the behavior of faceplates (flexural or shear stresses, buckling, yielding) for lateral loading. Figure 4(a) presents the strain gauge (S) layout for the exposed surfaces of the faceplates. Similar layout of strain gauges was used for the inside of the faceplate. High-temperature strain gauges were also installed in the

bottom region of the inside and outside faces of the flange plates. Type-K thermocouples were used to measure the surface temperatures and temperature through the thickness of the wall. The surface thermocouples [ST as shown in Figure 4(b)] were installed on the steel plates to control the ceramic heaters and to record the surface temperatures. Thermocouple trees [TT and CT in Figure 4(a)] were embedded in the concrete (placed in steel assembly before concrete casting) to measure the temperature through the thickness of the wall. A thermocouple tree consisted of



(a) Test unit details, strain gauge, and thermocouple tree layout



(b) String pots, clinometers, surface heaters, and surface thermocouples

Fig. 4. Sensor layout for test unit SC-W-H.

five thermocouples along the thickness of the wall (at 1, 2, and 5 in. from the surface of the wall). Layout of the heater assembly for the East faceplate is also shown in Figure 4(b) (Heater 1, 2, and 3).

## EXPERIMENTAL OBSERVATIONS AND RESULTS

Table 1 reports the material properties measured on the day-of-test for the test unit SC-W-H. The test unit SC-W-H was subjected to loading and heating protocols presented in Table 3, and histories summarized in Figure 2.

### Thermal Gradient

Figure 5(a) illustrates the evolution of through-thickness thermal gradient for surface temperature of 450°F [obtained from CT 6-10 in Figure 4(a)]. Even after 3 hr of heating, a nonlinear thermal gradient persisted through the wall thickness, with the wall center at approximately 265°F. The nonlinear thermal gradients and internal restraint resulted in thermally induced concrete cracking in the wall. For the case with surface temperature at 300°F (not included in Figure 5), the nonlinearity in the thermal gradient was lower and was reduced further as the duration of heating increased (after 3 hr of heating, the wall mid-thickness was about 230°F). An equivalent uniform through-thickness temperature of concrete infill can be estimated by assuming the thermal gradient distribution to be parabolic. The equivalent uniform concrete temperatures (for 3 hr heating) were 253°F and 326°F for surface temperatures of 300°F and 450°F, respectively.

### Force-Displacement

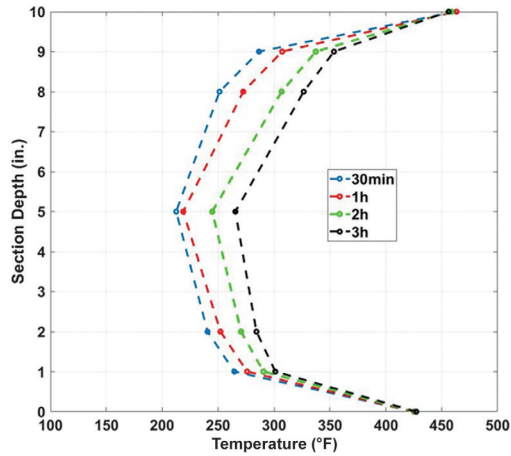
Figure 5(b) presents the lateral force-top displacement response of SC-W-H. The nominal in-plane shear strength ( $V_n^{AISC}$ , using measured properties) of the test unit, based on AISC N690 (2018) provisions is also indicated in the figure. The test unit reached an average peak load of 742 kips (+755 kips/–728 kips). Consistent with observations for heated specimens by Kitajima et al. (2017), the peak load for the test unit was 29% higher than  $V_n^{AISC}$ . This confirms that the strength of SC walls subjected to typical accident temperatures can be estimated conservatively using current U.S. code provisions. However, accident thermal loads did reduce the stiffness of the test units. Heated cycles (shown with solid red lines) are less stiff than the corresponding ambient cycles (shown with dotted black lines). In order to look closely at the stiffness reduction due to accident thermal loads, ambient and heated (3 hr duration)  $0.75F_n$  cycles are plotted in Figure 5(c). The heated cycles were less stiff than the ambient cycle, and the reduction in stiffness was higher for the cycle with surface temperature of 450°F. As

seen in Figure 5(b), the test unit exhibited pinched force-displacement hysteretic response after thermal loading. The hysteretic response for thermal cycles exhibited more extensive pinching than that typically observed at ambient temperatures because thermally induced strains result in the concrete crack widths to be larger. This resulted in a low initial stiffness, but the stiffness increased as compressive stresses (due to lateral loading) gradually closed the thermally induced cracks.

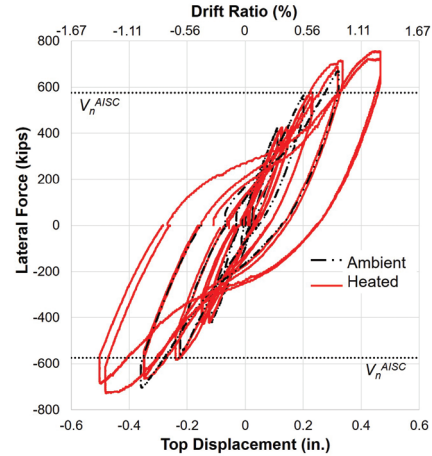
### Progression of Damage

Incremental lateral loading resulted in additional concrete flexural and shear cracking, followed by faceplate yielding in tension. Figure 5(d) presents the lateral force-longitudinal strain response of the faceplates for ambient and heated (450°F, 1 hr) cycles at  $0.75F_n$  and  $1.0\Delta_y$  (cycles 3, 6, and 8 and 10 in Table 3 and Figure 2). Strain gauges S3 and S10 were located at the base of the wall between the first and second row of studs [location of S10 shown in Figure 4(a); S3 was located on the opposite faceplate, corresponding to the location of S12 in Figure 4(a)]. Faceplates started yielding in tension during the ambient  $0.75F_n$  cycle, as S3 and S10 strains reached tensile strains of around 2000  $\mu\epsilon$  (net tensile strains in S3 and S10 were 1750 and 2300  $\mu\epsilon$ , respectively, compared to yield strain of 1980  $\mu\epsilon$ ). For the  $0.75F_n$  heated cycle, the net tensile strains were similar. There was no compression yielding in the faceplates for  $0.75F_n$  cycles. For the  $1.0\Delta_y$  heated and ambient cycles, the faceplate tensile strains exceeded the yield strain.

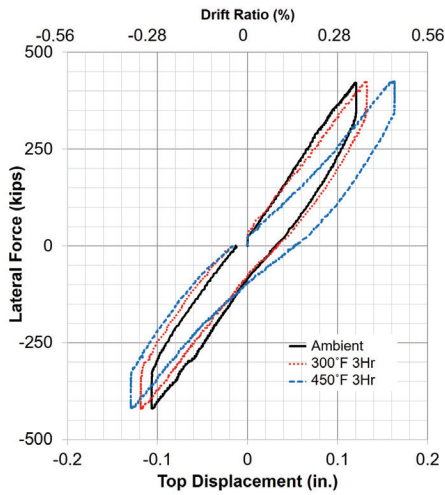
Because the test unit was designed to have a shear critical response, the flange plates were not expected to yield until after the  $\Delta_y$  cycles. Figure 5(e) presents the lateral force-longitudinal strain response of the flange plates for ambient  $0.75F_n$ ,  $1.0\Delta_y$  and  $1.5\Delta_y$  cycles (cycles 3, 10, and 13 in Table 3 and Figure 2). As the faceplate strains for ambient and heated cycles were similar [Figure 5(d)], only the ambient cycle strains have been plotted in Figure 5(e). Strain gauges S45 (north flange plate) and S47 (south flange plate) were installed between the bottom two rows of studs on flange plates, at 5 in. (125 mm) from the base. The flange plates did not undergo yielding for the cycles shown in the figure (tensile and compressive strains are lower than yield strain, 2070  $\mu\epsilon$ ). However, a reversal of incremental strains was observed during the  $1.5\Delta_y$  cycle [circled in Figure 5(e)]. Since the flange plate studs were detailed to ensure that the slenderness criteria of AISC N690 (2018) was satisfied, the flange plates were not expected to undergo buckling before compression yielding. However, as the lateral loading increased and the faceplates underwent von Mises yielding, the magnitude of concrete compression strut force anchored at the toe of the wall-to-baseplate connection (i.e., at the flange plate-faceplate-baseplate joint) increased. This compression strut, in combination with the vertical compressive



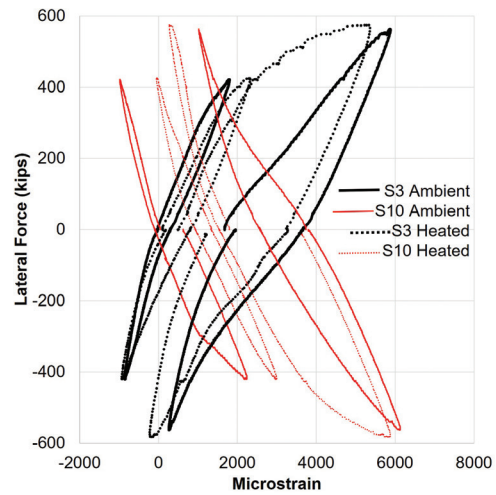
(a) Thermal gradient (surface at 232°C)



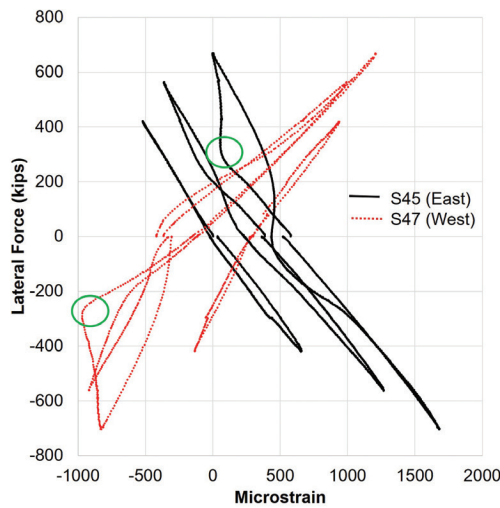
(b) Lateral force-top displacement ( $F-\Delta$ )



(c) Lateral force-top displacement (for  $0.75F_n$  cycles)



(d) Faceplate  $F-\epsilon$  for ambient and heated  $0.75F_n$  and  $\Delta_y$  cycles



(e) Flange plate  $F-\epsilon$  for ambient  $0.75F_n$ ,  $\Delta_y$  and  $1.5\Delta_y$  cycles

Fig. 5. Experimental results for SC-W-H.

force in flange plate (from the overturning moment induced by the lateral load), forced the flange plate (and faceplates near the corners) to bulge out between the bottom two rows of studs. This flange plate bulging resulted in the reversal of strains on the exterior face of flange plates [as observed in Figure 5(e)].

The concrete compression strut also caused additional stresses in the weld between the faceplate–flange plate–baseplate. These additional stresses at the weld location, compounded by the weld detail being highly constrained (due to discontinuities), resulted in the initiation of weld fracture at the corner joint during the second  $2\Delta_y$  cycle (cycle 13). The weld fracture is shown inset (top right) in Figure 6(a). The fracture progressed upward into the faceplate–flange plate weld and downwards into the flange plate–baseplate weld [shown in bottom right inset in Figure 6(a)]. This fracture resulted in faceplate and flange plate rupture and failure of the test unit in the next cycle. Steel rupture of the test unit is shown in Figure 6(a) (zoomed in to bottom of the test unit). The weld fracture [shown in top right inset in Figure 6(a)] propagated to fracture the flange plate and then the faceplates. The bulging of the faceplates due to the concrete compression strut (as discussed previously) is also visible in Figure 6(a).

After the failure of the test unit, one of the faceplates was removed to inspect the state of the concrete infill. Figure 6(b) shows the concrete cracking and damage in the test unit at failure. Concrete infill cracked predominantly in shear (the cracking angle varied between 35 and 45°). Rupture of the faceplates and flange plate at the base during the failure cycle resulted in the concrete infill being subjected to large rotation about the compression toe. This rotation caused large residual tensile strains and crack opening in the concrete, which is visible in Figure 6(b). Since the test unit failed due to plate rupture, there was no concrete compression crushing or faceplate shear buckling in the test unit.

### Stiffness Degradation

The lateral force–top displacement response of the test unit [Figures 5(b) and (c)] indicated a reduction in wall stiffness due to thermal loading. Because the test unit was shear controlled, the effect of thermal loads on the shear stiffness on the test unit is of particular interest. This shear stiffness of the test unit can be compared with stiffness provisions for analysis provided in AISC N690 (2018). Per AISC N690, shear stiffness of the SC wall depends on the magnitude of lateral loading. For lateral loads lower than a cracking threshold,  $S_{cr}^{AISC}$ , uncracked shear stiffness,  $GA_{uncr}^{AISC}$ , is considered. For lateral loads greater than  $2S_{cr}^{AISC}$ , the stiffness is considered to reduce to cracked secant stiffness,  $GA_{cr}^{AISC}$ , considering orthotropic cracked concrete and plane stress steel plate behavior. For lateral loads between  $S_{cr}^{AISC}$  and

$2S_{cr}^{AISC}$ , the stiffness can be linearly interpolated between uncracked and cracked stiffnesses. For thermal load combinations, the shear stiffness is considered to be cracked,  $GA_{cr}^{AISC}$ .

Figure 7(a) presents the lateral force–shear strain response of the test unit (for  $0.25F_n$  and  $0.5F_n$  ambient cycles), where the slope of the response is the experimentally observed shear stiffness. Shear strain for the test unit was calculated from strain gauge rosettes (S4-6, S7-9, S13-15, S16-18). The location of strain gauges S13-18 is shown in Figure 4(a). S4-9 were located on the other faceplate at locations corresponding to S13-18 in Figure 4(a). The strain values from rosettes were used to obtain principal strains and direction. Shear strain,  $\gamma_{xy}$ , was calculated using the principal strains and direction. Average shear strain for the four strain gauge rosettes was plotted in Figure 7(a). The figure includes lines corresponding to the secant shear stiffness estimated using AISC provisions—namely,  $GA_{uncr}^{AISC}$ ,  $GA_{cr}^{AISC}$ , and a line corresponding to  $GA_{cr}^{TAN}$ , which is the tangent cracked shear stiffness for SC walls estimated using equations in Seo et al. (2016), also discussed in the AISC N690 commentary.

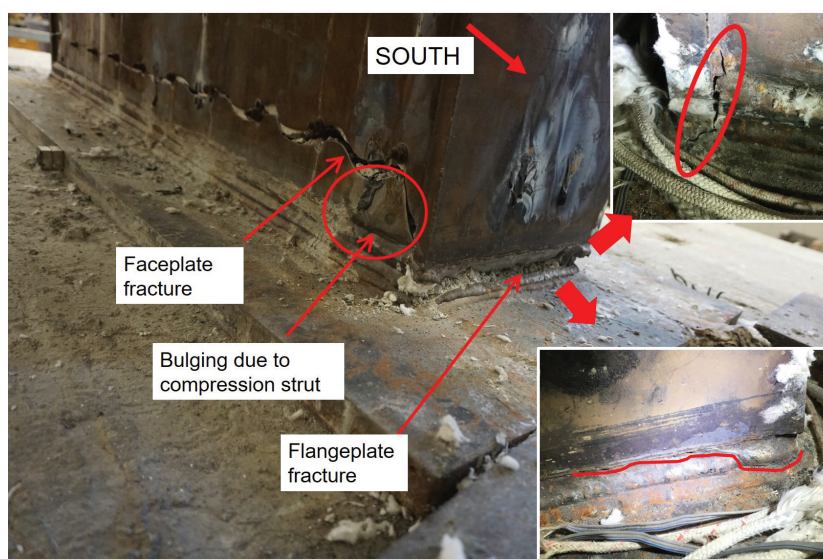
It is observed that the uncracked stiffness,  $GA_{uncr}^{AISC}$ , was not manifest in the test unit (even at ambient conditions). This may be due to shrinkage-related cracking and concrete cracking at low magnitude of lateral loads. The test unit developed shear cracks at force level approximately equal to  $S_{cr}^{AISC}$ , and the stiffness reduced further thereafter. Shear stiffness for the  $0.25F_n$  cycle was approximately equal to the cracked secant stiffness,  $GA_{cr}^{AISC}$ . For the  $0.5F_n$  cycle, the stiffness dropped below  $GA_{cr}^{AISC}$ . However, the shear stiffnesses for both the cycles were higher than the tangent cracked stiffness,  $GA_{cr}^{TAN}$ . This suggests that the lower-bound shear stiffness of the test unit can be estimated as  $GA_{cr}^{TAN}$ . AISC recommended secant stiffness,  $GA_{cr}^{AISC}$ , was higher than experimentally observed secant stiffness. This may be because the uncracked stiffness was not manifest (or the test unit cracked at low magnitude of lateral force).

Figure 7(b) presents the degradation of the experimentally measured shear stiffness of the test unit, where the measured shear stiffness is normalized with the cracked tangent stiffness,  $GA_{cr}^{TAN}$ . The experimental shear stiffness was estimated using data from the strain gauge rosettes [as discussed for Figure 7(a)]. The shear stiffness of the test unit was also estimated using lateral displacement measurements in order to cross-check the values estimated using strain gauge rosettes and to obtain stiffness values for cycles where strain gauges were damaged due to heating. The corrected top displacement values (corrected for rigid body displacements associated with base slip and rotation) consist of both shear and flexural deflections. The flexural deflection was estimated using  $EI_{cr}$  (cracked flexural stiffness). For calculation of  $EI_{cr}$ , the neutral axis location was considered to be at one-third of the length of the test unit (consistent with observations based on strain gauge data

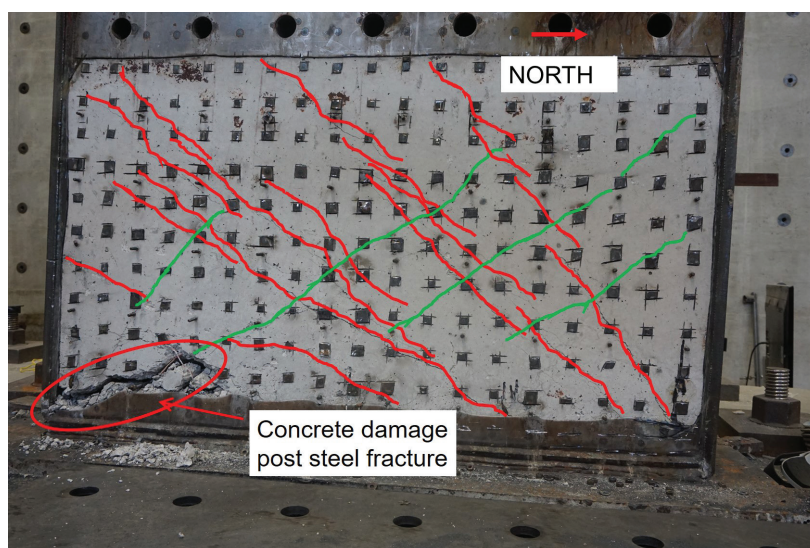
and the cross-section moment curvature relationship). For heated cycles, the flexural stiffness is considered to linearly reduce from  $EI_{cr}$  to  $EI_{steel}$  for surface temperature increase,  $\Delta T$ , from 0°F to 270°F (based on the observations and recommendations discussed later). The shear deflection was then calculated by subtracting the flexural deflection from the total deflection, and the shear strain was estimated as the shear deflection divided by the test unit loading height. The shear stiffnesses estimated using the strain gauge data, and lateral displacement data are compared in Figure 7(b).

For the pre-yield  $0.5F_n$  and  $0.75F_n$  ambient cycles, the shear stiffness estimated using the lateral displacement data

is slightly higher than the stiffness estimated using strain gauge data, but the trends are similar. For the  $0.75F_n$ , 300°F cycles, some of the strain gauge rosettes were damaged due to heating, and the average shear strain consists of only the functioning rosettes. For the  $1.0\Delta_y$  cycles, stiffnesses estimated using displacement data are slightly higher because the test unit was undergoing shear yielding, which was not considered in displacement data stiffness calculations. Based on the comparisons in Figure 7(b), the stiffnesses estimated using lateral displacement data can be considered cautiously in the absence of complete or adequate strain gauge data.



(a) Steel failure



(b) Concrete cracking

Fig. 6. Test unit SC-W-H at failure.

As observed in Figures 7(a) and 7(b), the shear stiffness for the  $0.25F_n$  and  $0.5F_n$  ambient cycles was higher than the cracked tangent shear stiffness,  $GA_{cr}^{TAN}$ . The ambient shear stiffness corresponding to  $0.75F_n$  was approximately equal to  $GA_{cr}^{TAN}$ . However, the normalized stiffness for  $0.75F_n$  cycles dropped considerably as thermal loading was applied. The normalized stiffness reduction was 21% for 300°F and 38% for 450°F in comparison to the ambient stiffness. As mentioned earlier, the reduction in normalized stiffness can be attributed to (1) the temperature-dependent reduction in elastic and shear moduli of steel and concrete materials and (2) concrete cracking effects. Calculations indicate that the stiffness reduction due to item 1 is 16% for 300°F and 26% for 450°F. The remaining reduction is due to item 2, which is concrete cracking induced by thermal strains, nonlinear gradient, and internal restraint. These experimental results, observations, and discussion indicate that the reduction in shear stiffness due to items 1 and 2 needs to be considered for seismic and thermal loading combinations. Figure 7(b) also includes a horizontal line corresponding to the ambient shear stiffness of the steel alone,  $GA_{steel}$ , while ignoring the contribution of the concrete infill due to extensive cracking. Based on Figure 7(b), the shear stiffness can be considered to reduce linearly from  $GA_{cr}^{TAN}$  to  $GA_{steel}$  for a surface temperature increase,  $\Delta T$ , from 0°F to 270°F. This would provide a lower-bound estimate of the shear stiffness and also eliminate the need for using temperature-dependent properties for typical accident temperatures.

The overall stiffness response of the SC wall is a combination of its flexural and shear stiffnesses. The stiffness degradation of the SC-W-H test unit was evaluated by considering the reduction of the normalized stiffness,  $K_{sec}/K_{cr}$ , with loading and heating cycles. The secant stiffness,  $K_{sec}$ , was calculated as the average of push (+) and pull (–) stiffnesses. The push and pull stiffnesses were calculated from the peak force and corresponding displacement values (corrected for base slip and base rotation) for a cycle. The cracked stiffness,  $K_{cr}$ , was calculated using the cracked flexural and shear stiffness—namely,  $EI_{cr}$  and  $GA_{cr}^{TAN}$ .  $EI_{cr}$  was calculated considering the neutral axis at one-third of the test unit length (as discussed previously). Figure 7(c) presents the degradation of the normalized secant stiffness,  $K_{sec}/K_{cr}$ , of the test unit with loading and heating cycles. As observed previously in Figure 7(a), the uncracked stiffness did not manifest in the wall (even for the initial cycles). The secant stiffness,  $K_{sec}$ , of the wall for  $0.25F_n$  cycles was 1.9 times  $K_{cr}$  (which is also 0.52 times the uncracked stiffness). The secant stiffness reduced for higher lateral loads as the concrete developed shear and flexural cracks. The secant stiffness corresponding to  $0.75F_n$  ambient cycles was approximately equal to  $0.9K_{cr}$ .

As shown in Figure 7(c), accident thermal loading reduced the normalized stiffness significantly. The secant

stiffness reduced to  $0.70K_{cr}$  for the  $0.75F_n$ , 300°F cycles and to  $0.58K_{cr}$  for the  $0.75F_n$ , 450°F cycles. The duration of heating (1 hr or 3 hr) did not seem to have a significant influence on the normalized stiffness because concrete cracking occurs early upon the introduction of heating due to the nonlinear thermal gradient and internal restraints. While the additional heating duration reduces the nonlinearity of the thermal gradient, it does not result in an increase in the stiffness. To evaluate any change in stiffness upon cooling down of specimens, ambient cycles were performed after the heated cycles (i.e., the test unit was allowed to cool down) for the  $1.0\Delta_y$  and  $1.5\Delta_y$  displacement levels. The normalized ambient stiffness for the  $1.0\Delta_y$  cycle is 20% higher than normalized heated stiffness. Similarly, for the  $1.5\Delta_y$  cycle, the ambient stiffness is marginally higher than heated stiffness.

## EVALUATION OF SC WALL BEHAVIOR AND RECOMMENDATIONS

### Thermal Gradient

The specimens tested by Kitajima et al. (2017) were subjected to surface temperatures ranging from 293°F to 572°F for heating duration of 30 days (Specimen 4 was heated for 60 min). The specimens (except Specimen 4) were expected to develop uniform temperature distribution through the thickness [based on Bhardwaj et al. (2015)]. No information was provided regarding the through thickness thermal gradients. The unit tested by the authors was subjected to two surface temperature magnitudes (300°F and 450°F) and two heating durations (1 hr and 3 hr). A nonlinear thermal gradient developed through the wall thickness due to the thermal loads. The extent of nonlinearity reduced as the duration of heating increased. The thermal gradient was higher for surface temperature of 450°F. The mid-thickness of the test unit was at 265°F corresponding to a surface temperature of 450°F and heating duration of 3 hr. The nonlinear thermal gradient resulted in concrete-cracking due to self-restraint and external restraints, which reduced the stiffness of the test unit.

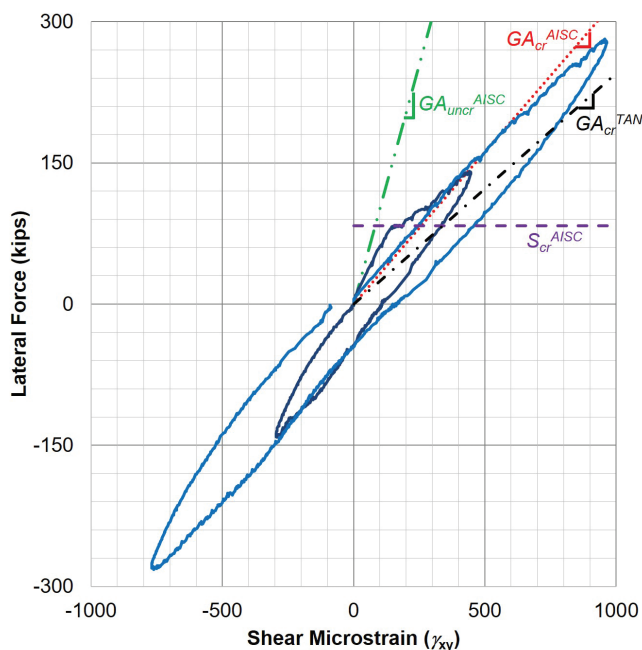
### Strength and Stiffness

Table 4 presents the summary of experimental results discussed in the paper. The table presents the maximum surface temperature,  $T_{max}$ , maximum increase in surface temperature ( $\Delta T_{max}$ , considering ambient temperature of 68°F), measured lateral strength,  $V_{n-ip}$ , and the ratios of measured strength with nominal strength per AISC N690 ( $V_n^{AISC}$ , using measured properties) and the ultimate shear strength ( $V_u$ ) per Booth et al. (2020). The strength of the heated specimens tested by Kitajima et al. (2017) was higher than the nominal in-plane shear strength (using

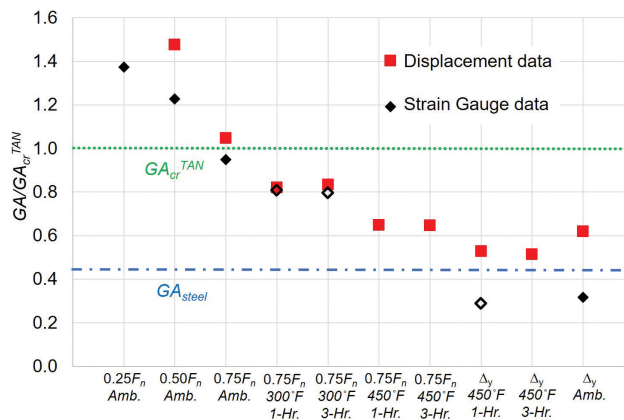
measured properties) per AISC N690 (2018), with a safety margin ranging from 9% to 36%. The experiments indicated that the strength of SC wall specimens reduced by 15 to 30% for accident thermal loads in comparison to strength of the ambient specimen. Additionally, the strengths of the heated specimens were up to 15% lower than the calculated ultimate shear strength at ambient conditions per Booth et al. (2020). The measured peak strength for the test unit SC-W-H was 29% higher than  $V_n^{AISC}$  (about 25% lower than the ultimate shear strength). Based on the experimental results,

the strength of specimens subjected to typical accident thermal temperatures and durations can be conservatively estimated using existing strength equations (per U.S. codes, based on von Mises yielding of steel plates) for ambient conditions.

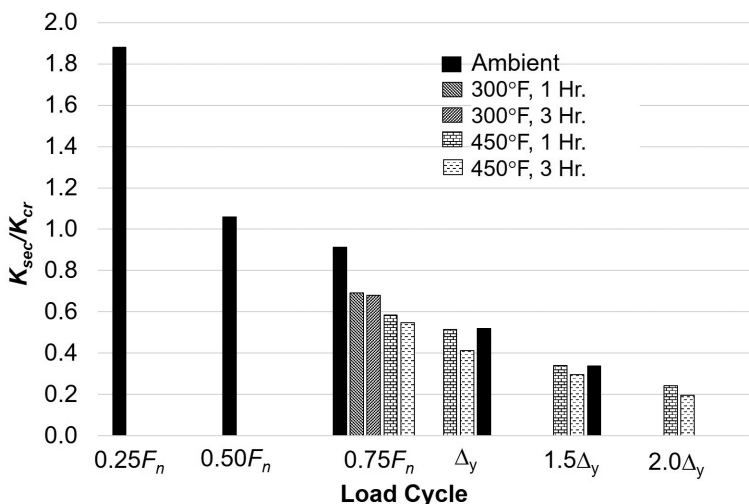
Table 4 also presents the normalized initial,  $K_{in}$ , and secant stiffnesses,  $K_{sec}$ , and the corrected failure drift ratio for the specimens and the test unit. Initial stiffness of the specimens is normalized with theoretical uncracked stiffness,  $K_{un-cr}$ , for the specimens.  $K_{un-cr}$  is calculated considering



(a) Shear stiffness:  $0.25F_n$  and  $0.5F_n$  cycles



(b) Shear stiffness degradation



(c) Secant stiffness degradation

Fig. 7. Shear and wall secant stiffness for SC-W-H.

**Table 4. Summary of Experimental Results**

Identifier <sup>1</sup>	$T_{max}$ (°F)	$\Delta T_{max}$ (Δ°F)	$V_{n-ip}$ (kips)	$V_{n-ip}/V_n^{AISC}$	$V_{n-ip}/V_u$	$K_{in}/K_{uncr}$	$K_{sec}/K_{cr}$	Drift Ratio Failure (%)	$K_{sec}/K_{eff}$
2	Ambient	NA	790	1.54	1.08	0.67	0.95	2.3	0.95
3	293	225	561	1.09	0.84	0.29	0.62	4.3	1.02
4	293	225	699	1.36	0.94	0.23	0.61	4.6	1.01
5	347	279	600	1.17	0.87	0.22	0.55	4.0 <sup>2</sup>	1.11
7	572	504	609	1.18	0.95	0.20	0.50	4.0 <sup>2</sup>	1.04
SC-W-H	Ambient	NA	742 <sup>3</sup>	1.29	0.72	0.52	0.91	1.17 <sup>3</sup>	0.91
	300	232				—	0.68		1.13
	450	382				—	0.55		1.10

<sup>1</sup> Specimens 2–5 and 7 were tested by Kitajima et al. (2017); test unit SC-W-H was tested by the authors.  
<sup>2</sup> The force-displacement response beyond this drift not presented in Kitajima et al. (2017).  
<sup>3</sup> Specimen failure initiated by weld fracture.

uncracked shear and flexural stiffnesses of the specimens. Experimental results indicate that uncracked stiffness was not manifest in the specimens (even at ambient conditions). This may be due to shrinkage-induced cracking in the concrete and the concrete cracking in the test unit at low magnitude of lateral loads. The stiffness of the ambient specimens reduced further as the magnitude of shear force applied exceeded the cracking threshold.

Heated specimens by Kitajima et al. (2017) indicated a reduction of 60 to 70% in initial stiffness due to accident thermal loading. Secant stiffness of the specimens is normalized with theoretical cracked stiffness,  $K_{cr}$ , of the specimens (without considering temperature dependent properties). Calculation of  $K_{cr}$  was discussed previously (it can also be calculated by cross-section moment-curvature analysis). Since the specimens tested by Kitajima et al. were similar to the test unit SC-W-H, the neutral axis location for those specimens is also considered at one-third of the specimen length (confirmed with cross-section moment-curvature analysis). Ambient secant stiffness of SC wall specimens can be reasonably estimated as  $K_{cr}$ . Accident thermal loads significantly reduce the stiffness of the specimens. The extent of reduction in stiffness depends on the temperature magnitude of thermal accident. Heated specimens tested by Kitajima et al. experienced a secant stiffness reduction of up to 50% in comparison to secant stiffness for ambient specimen. Heated secant stiffness (and shear stiffness) for test unit SC-W-H reduced by about 25% for 300°F and 40% for 450°F, in comparison to ambient secant (and shear) stiffness. Kitajima et al. specimens failed at drift ratios ranging from 2.3 to 4.6% with significant post-peak ductility. SC-W-H failed due to weld fracture, but still reached a drift ratio of 1.17%.

Based on the experimental results, the secant stiffness (flexure and shear stiffness) for shear-controlled SC walls can be considered to linearly reduce from cracked stiffness to steel-only stiffness for surface temperature change,  $\Delta T$ , from 0°F to 270°F. The effective in-plane flexural and shear stiffnesses for SC walls can be calculated as shown in Equations 1 and 2, respectively (all values in U.S. units). While the equations are consistent with those proposed for SC wall piers (Bhardwaj et al., 2019a), the calculation of individual terms is different for SC walls and SC wall piers.

$$EI_{eff} = EI_{cr} - \frac{(EI_{cr} - E_s I_s)}{270} \Delta T \geq E_s I_s \quad (1)$$

$$GA_{eff} = GA_{cr}^{TAN} - \frac{(GA_{cr}^{TAN} - G_s A_s)}{270} \Delta T \geq G_s A_s \quad (2)$$

Table 4 also presents the comparison of secant stiffnesses for the specimens normalized with recommended effective stiffnesses,  $K_{sec}/K_{eff}$ .  $K_{eff}$  is calculated considering  $EI_{eff}$  and  $GA_{eff}$  as recommended in Equations 1 and 2. The secant (ambient and heated) stiffnesses of the specimens can be reasonably estimated using the recommendations. Because the recommended stiffness reductions provide lower-bound estimates of stiffness, they eliminate the need to consider temperature-dependent properties (for typical accident temperatures up to 572°F). The stiffness recommendations are based on the experiments discussed in this paper. Further experimental or numerical research is needed to validate the recommendations for range of parameters not considered in this paper. The recommended stiffness values can be used to conduct analyses for seismic and accident thermal loading combination per AISC N690 (2018) and as illustrated in Bhardwaj and Varma (2017).

## CONCLUSIONS

Steel-plate composite walls in labyrinthine safety-related nuclear facilities need to be designed for combination of accident thermal scenarios with design basis shaking. This paper describes the experimental results for SC walls subjected to combination of accident thermal temperature and seismic loads. The results of SC wall specimens tested by Japanese researchers and the unit tested by the authors were presented in this paper. The following conclusions can be drawn from the experiments:

Based on the data available in design control documents, typical accident temperatures for nuclear facilities may range from 300°F to 570°F, with the temperatures maintained for up to a few days after the accident. The thermal accidents result in the evolution of nonlinear thermal gradients through the cross section. The thermal gradients are highly nonlinear for the first few hours after the accident, and the extent of nonlinearity reduces as the concrete temperature increases with time.

The nominal in-plane shear strength of SC walls at ambient temperatures can be conservatively estimated using the provisions of AISC N690 (2018), which correspond to the limit state of von Mises yielding of the steel faceplates. The ultimate in-plane shear strength of SC walls at ambient temperatures may be calculated using equations by Booth et al. (2020). The in-plane shear strength of specimens subjected to typical accident thermal temperatures (up to 570°F) and durations should be limited to that calculated using the current AISC N690 strength equations for ambient temperatures (based on von Mises yielding of the steel plates); that is, the Booth et al. (2020) equations cannot be used for calculating in-plane shear strength at accident thermal temperatures.

Ambient secant stiffness of SC walls can be reasonably estimated considering cracked flexural,  $EI_{cr}$ , and shear stiffnesses,  $GA_{cr}$ .  $EI_{cr}$  can be calculated from the moment-curvature relationship, and  $GA_{cr}$  can be estimated as the tangent shear stiffness,  $GA_{cr}^{TAN}$ , based on composite plate theory (Seo et al., 2016). The stiffness of SC walls may be significantly reduced depending on the magnitude of surface temperature and the duration of the accident. The SC unit tested by the authors exhibited reduction in secant stiffness (and shear stiffness) of 25% for surface temperature of 300°F and 40% for surface temperature of 450°F in comparison to the ambient secant stiffness.

The specimens tested by Kitajima et al. (2017) exhibited stiffness reductions of up to 50% of the ambient secant stiffnesses. The reduction in stiffness is due to concrete cracking and reduced elastic and shear moduli of the steel and concrete at elevated temperatures. Concrete cracking also leads to higher stress in steel plates, which may cause the steel plates to yield at lower loads. The stiffness reduction due to accident thermal loads can be considered in analysis

by using effective flexure and shear stiffnesses. The effective stiffnesses can be assumed to linearly reduce from cracked stiffness to steel-only stiffness for surface temperature change,  $\Delta T$ , from 0°F to 270°F. The effective stiffness recommendations are based on the experimental studies discussed in this paper. Additional experimental or numerical research is recommended to further verify and improve the applicability of these recommendations for range of parameters not considered in this paper. For example, this article does not consider the effect of one-sided heating on the strength and stiffness of SC walls. Additional studies are needed to evaluate these effects.

## DATA AVAILABILITY STATEMENT

The data for the unit tested by the authors (SC-W-H) are available from the corresponding author by request. The data for the tests conducted by the Japanese researchers, which are used in this paper, are obtained from their publications (Hirama et al., 2015; Kitajima et al., 2017).

## ACKNOWLEDGMENTS

The research presented in this article was funded through the FY 2014 Nuclear Energy Enabling Technologies Research & Development and Infrastructure Awards by the U.S. Department of Energy, grant number DOE-ID-14-032. The authors thank Mr. Tom Bradt for his assistance in conducting the tests at Bowen Laboratory.

## REFERENCES

- ACI (2013), *Code Requirements for Nuclear Safety-Related Concrete Structures and Commentary*, ACI 349, American Concrete Institute, Farmington Hills, Mich.
- AISC (2016), *Seismic Provisions for Structural Steel Buildings*, ANSI/AISC 341-16, American Institute of Steel Construction, Chicago, Ill.
- AISC (2018), *Specification for Safety-Related Steel Structures for Nuclear Facilities*, ANSI/AISC N690-18, American Institute of Steel Construction, Chicago, Ill.
- Alzeni, Y. and Bruneau, M. (2014), "Cyclic Inelastic Behavior of Concrete Filled Sandwich Panel Walls Subjected to In-Plane Flexure," *Technical Report MCEER-14-0009*, MCEER, University at Buffalo, Buffalo, N.Y.
- Anwar, H.S., Bhardwaj, S.R., and Varma, A.H. (2019), "On the Response of Squat Reinforced Concrete Walls for Combined Lateral and Accident Thermal Loading," *Proceedings of SMiRT25*, IASMiRT, Charlotte, N.C. <https://www.lib.ncsu.edu/resolver/1840.20/37803>
- ASCE (2022), *Minimum Design Loads for Buildings and Other Structures*, ASCE 7-22, American Society of Civil Engineers, Reston, Va.

- Bhardwaj, S.R. (2018), "Multi-Hazard In-Plane Response of Steel-Plate Composite Walls: Out-of-Plane and Accident Thermal Loadings," *Open Access Dissertations*, 1689, Purdue University, West Lafayette, Ind. [https://docs.lib.purdue.edu/open\\_access\\_dissertations/1689](https://docs.lib.purdue.edu/open_access_dissertations/1689)
- Bhardwaj, S.R., Sener, K.C., and Varma, A.H. (2018), "Experimental Evaluation of Structural Walls for Seismic and Thermal Forces," in *Proceedings of 11th U.S. National Conference on Earthquake Engineering*, Los Angeles, Calif.
- Bhardwaj, S.R., Sener, K.C., and Varma, A.H. (2019a), "Multi-Hazard Investigation and Testing of Steel-Plate Composite (SC) Wall Piers: Seismic and Thermal Loads," *Nuclear Engineering and Design*, Vol. 348, pp. 121–130, Elsevier. DOI: 10.1016/j.nucengdes.2019.03.026
- Bhardwaj, S.R. and Varma, A.H. (2017), *Design of Modular Steel-Plate Composite Walls for Safety-Related Nuclear Facilities*, Design Guide 32. American Institute of Steel Construction, Chicago, Ill. <https://www.aisc.org/Design-Guide-32-Modular-Steel-Plate-Composite-Walls-for-Safety-Related-Nuclear-Facilities>
- Bhardwaj, S.R., Varma, A.H., and Orbovic, N. (2019b), "Behavior of Steel-Plate Composite Wall Piers under Biaxial Loading," *Journal of Structural Engineering*, ASCE, Vol. 145, No. 2. [https://doi.org/10.1061/\(ASCE\)ST.1943-541X.0002247](https://doi.org/10.1061/(ASCE)ST.1943-541X.0002247)
- Bhardwaj, S.R., Varma, A.H., and Sener, K.C. (2015), "On the Calculation of Design Demands for Accident Thermal Loading Combination," *Transactions of SMiRT 23* in Manchester, UK, Paper ID 850, *IASMiRT*, North Carolina State University, Raleigh, N.C., pp. 1–10. <http://www.lib.ncsu.edu/resolver/1840.20/34279>
- Booth, P.N., Bhardwaj, S.R., Tseng, T., Seo, J., and Varma, A.H., (2020), "Ultimate Shear Strength of Steel-Plate Composite (SC) Walls with Boundary Element," *Journal of Constructional Steel Research*, Vol. 165, Elsevier Science. <https://doi.org/10.1016/j.jcsr.2019.105810>
- Booth, P.N., Varma, A.H., Sener, K., and Malushte, S. (2015), "Flexural Behavior and Design of Steel-Plate Composite (SC) Walls for Accident Thermal Loading," *Nuclear Engineering and Design*, Vol. 295, pp. 817–828, Elsevier Science. <http://dx.doi.org/10.1016/j.nucengdes.2015.07.036>
- Bruhl, J. and Varma, A.H. (2018), "Experimental Evaluation of Steel-Plate Composite Walls Subject to Blast Loads," *Journal of Structural Engineering*, ASCE, Vol. 144, No. 9. DOI: 10.1061/(ASCE)ST.1943-541X.0002163
- Bruhl, J., Varma, A.H., and Johnson, W.H. (2015), "Missile Impact Behavior and Design of Composite SC Walls," *International Journal of Impact Engineering*, Vol. 75, pp. 75–87, Elsevier Science. <http://dx.doi.org/10.1016/j.ijimpeng.2014.07.015>
- Bruneau, M., Alzeni, Y., and Fouché, P. (2013), "Seismic Behavior of Concrete-Filled Steel Sandwich Walls and Concrete-Filled Steel Tube Columns," *Steel Innovations 2013 Conference*, Christchurch, New Zealand.
- CEN (2004), *Eurocode 2: Design of Concrete Structures—Part 1–2: General Rules—Structural Fire Design*, Comité Européen de Normalisation, EN-1992-1-2, Brussels, Belgium.
- CEN (2005), *Eurocode 3: Design of Steel Structures—Part 1–2: General Rules—Structural Fire Design*, Comité Européen de Normalisation, EN-1993-1-2, Brussels, Belgium.
- Hirama, T., Kumagai, H., Tanabe, M., Saigou, S., Sawada, S., and Akase, T. (2015), "Applicability Evaluation of Steel Plate Reinforced Concrete Structure to Primary Containment Vessel of BWRs: (2) Mechanical and Thermal Properties of Steel under High Temperature Conditions," *Transactions of SMiRT 23*, IASMiRT, Manchester, U.K.
- Hong, S. and Varma, A.H. (2009), "Analytical Modeling of the Standard Fire Behavior of Loaded CFT Columns," *Journal of Constructional Steel Research*, Vol. 65, No. 1, pp. 54–69.
- Ji, X., Cheng, X., Jia, X., and Varma, A.H. (2017), "Cyclic In-Plane Shear Behavior of Double-Skin Composite Walls in High-Rise Buildings," *Journal of Structural Engineering*, ASCE, Vol. 143, No. 6. [https://doi.org/10.1061/\(ASCE\)ST.1943-541X.0001749](https://doi.org/10.1061/(ASCE)ST.1943-541X.0001749)
- Kitajima, Y., Tanabe, M., Hirako, S., Hirma, T., Kumagai, H., and Abiru, T. (2017), "Applicability Evaluation of Steel Plate Reinforced Concrete Structure to Primary Containment Vessel of BWRs: (8) Shear Loading Test of Steel Plate Reinforced Concrete Structure under High Temperature Conditions," *Transactions of SMiRT 24*, IASMiRT, Busan, Republic of Korea.
- Kodur, V., Dwaikat, M., and Fike, R. (2010), "High Temperature Properties of Steel for Fire Resistance Modeling of Structures," *Journal of Material and Civil Engineering*, Vol. 22, pp. 423–434.
- Kurt, E.G., Varma, A.H., Booth, P.N., and Whittaker, A. (2016), "In-Plane Behavior and Design of Rectangular SC Wall Piers without Boundary Elements," *Journal of Structural Engineering*, ASCE, Vol. 142, No. 6.

- Naus, D.J. (2009), "A Compilation of Elevated Temperature Concrete Material Property Data and Information for Use in Assessments of Nuclear Power Plant Reinforced Concrete Structures," Oak Ridge National Laboratory, prepared for U.S. Nuclear Regulatory Commission.
- NRC (2011), "Design Control Document for AP1000," U.S. Nuclear Regulatory Commission, Washington, D.C.
- NRC (2012), "Design Control Document for US-APWR," U.S. Nuclear Regulatory Commission, Washington, D.C.
- NRC (2020, May), "Safety-Related Concrete Structures for Nuclear Power Plants (Other than Reactor Vessels and Containments)," *Regulatory Guide 1.142*, Rev. 3, U.S. Nuclear Regulatory Commission, Washington, D.C.
- NRC (2021, August), "Safety-Related Steel Structures and Steel-Plate Composite Walls for Other Than Reactor Vessels and Containments," *Regulatory Guide 1.243*, Rev. 0, U.S. Nuclear Regulatory Commission, Washington, D.C.
- Ozaki, M., Akita, S., Oosuga, H., Nakayama, T., and Adachi, N. (2004), "Study on Steel Plate Reinforced Concrete Panels Subjected to Cyclic In-Plane Shear," *Nuclear Engineering and Design*, Vol. 228, pp. 225–244.
- Schlaseman, S. and Russell, J. (2004), "Application of Advanced Construction Technologies to New Nuclear Power Plants," *Report MPR-2610*, Rev. 2, Report for U.S. Department of Energy, under contract for DE-AT01-02NE23476.
- Selvarajah, R. (2013), "Behavior and Design of Earthquake-Resistant Dualplate Composite Shear Wall Systems," Doctoral Dissertation, Purdue University, West Lafayette, Ind.
- Sener, K.C., Bhardwaj, S.R. and Varma, A.H. (2019a), "Effects of Accident Thermal Loading on Shear Behavior of Reinforced Concrete Members," *ACI Structural Journal*, Vol, 116, No. 3. DOI: 10.14359/51713305.
- Sener, K.C., Varma, A.H., and Bhardwaj, S.R. (2015a), "Accident Thermal Loading Effects on Seismic Behaviour of Safety-Related Nuclear Structures," *Transactions of SMiRT 23*, Paper ID 701, IASMiRT, Manchester, UK, pp. 1–10.
- Sener, K., Varma, A.H., Booth, P.N., and Fujimoto, R. (2015b), "Seismic Behavior of a Containment Internal Structure Consisting of Composite SC Walls," *Nuclear Engineering and Design*, Vol. 295, pp. 804–816, Elsevier Science. <http://dx.doi.org/10.1016/j.nucengdes.2015.07.038>
- Sener, K.C., Varma, A.H., and Chu, M. (2019b), "Seismic Performance of an Idealized Steel-Plate Composite (SC) Structure Subjected to Accident Thermal Loading," *Nuclear Engineering and Design*, Vol. 352. <https://doi.org/10.1016/j.nucengdes.2019.05.029>
- Seo, J., Varma, A.H., Sener, K. and Ayhan, D. (2016), "Steel-Plate Composite (SC) Walls: In-Plane Shear Behavior, Database, and Design," *Journal of Constructional Steel Research*, Vol. 119, pp. 202–215, Elsevier Science. <http://dx.doi.org/10.1016/j.jcsr.2015.12.013>
- Simulia (2014), *ABAQUS 6.14 Documentation*, Dassault Systemes Simulia Corporation Providence, R.I.
- Takeuchi, M., Hiramoto, M., Kumagai, N., Yamazaki, N., Kodaira, A., and Sugiyama, K. (1993), "Material Properties of Concrete and Steel Bars at Elevated Temperatures," *Transactions of SMiRT12*.
- Varma, A.H., Lai, Z., and Seo, J. (2017), "An Introduction to Coupled Composite Core Wall Systems for High-Rise Construction," *Proceedings of the 8th International Conference on Composite Construction in Steel and Concrete*, Wyo.
- Varma, A.H., Malushte, S.R., and Lai, Z., (2015), "Modularity & Innovation Using Steel-Plate Composite (SC) Walls for Nuclear and Commercial Construction," *Proceedings of the 11th International Conference on Advances in Steel-Concrete Composite Structures (ASCCS)*, Tsinghua University, Beijing, China. <http://dx.doi.org/10.13140/RG.2.1.4665.4804>
- Varma A.H., Malushte S.R., Sener K., and Lai Z. (2014), "Steel-Plate Composite (SC) Walls for Safety Related Nuclear Facilities: Design for In-Plane Force and Out-of-Plane Moments," *Nuclear Engineering and Design*, Vol. 269, pp. 240–249, Elsevier Science. <http://dx.doi.org/10.1016/j.nucengdes.2013.09.019>
- Vecchio, F J. and Sato, J.A. (1990), "Thermal Gradient Effects in Reinforced Concrete Frame Structures," *ACI Structural Journal*, Vol. 87, No. 3, pp. 262–275.
- Zhang, K., Varma, A.H., Malushte, S.R., and Gallocher, S. (2014), "Effect of Shear Connectors on Local Buckling and Composite Action in Steel Concrete Composite Walls," *Nuclear Engineering and Design*, Vol. 269, pp. 231–239, Elsevier Science. <http://dx.doi.org/10.1016/j.nucengdes.2013.08.035>